RSC Advances

PAPER

View Article Online
View Journal | View Issue

Cite this: *RSC Adv.*, 2025, **15**, 43792

Comprehensive analysis of antimony-based organic–inorganic hybrid material: phase transition, Raman scattering, and the electrical conduction mechanism of $[(CH_3)_4P]_3Sb_2Br_9$

Khaoula Ben Brahim, [a] Arafat Ghoudi, [a] Ines Mbarek,[a] Noweir Ahmad Alghamdi,[b] Malika Ben Gzaiel[a] and Abderrazek Oueslati *[a]

The present work focuses on elucidating the origin of the phase transition in $[(CH_3)_4P]3Sb_2Br_9$ and its associated electrical properties. The compound was synthesized by slow solvent evaporation at constant temperature and characterized using X-ray powder diffraction, FTIR spectroscopy, temperature-dependent Raman spectroscopy, and impedance spectroscopy. XRD confirmed the formation of a monoclinic structure with the polar $P3_1c$ space group. Complementary FTIR and Raman analyses enabled the assignment of vibrational modes at room temperature, providing a reliable reference for monitoring temperature-induced phase transitions. Raman spectra collected between 294 and 563 K revealed specific molecular displacements and reorientations of both organic and inorganic components associated with the transition near 540 ± 7 K. Impedance spectroscopy in the 433–563 K range displayed a single semicircle in the Nyquist plots, evidencing a grain-dominated electrical response. The impedance data were successfully modeled by an equivalent circuit comprising a resistance in parallel with a constant phase element. Both ac and dc conductivities were analyzed to clarify the conduction mechanisms, with charge transport found to obey Jonscher's power law and consistent with the Correlated Barrier Hopping (CBH) and Non-overlapping Small Polaron Tunneling (NSPT) models. $[(CH_3)_4P]_3Sb_2Br_9$ shows both phase transition and ionic conduction, highlighting its potential in memory devices, electrolytes, light-harvesting, and energy applications.

Received 11th September 2025
Accepted 5th November 2025

DOI: 10.1039/d5ra06870c

rsc.li/rsc-advances

1. Introduction

Organic–inorganic hybrid materials have attracted substantial attention due to their unique properties and broad range of potential applications in fields such as electronics, photonics, biomedicine, energy harvesting, and renewable energy systems.[1–4] These materials combine the mechanical robustness, optical transparency, and thermal stability of inorganic components with the flexibility, lightweight nature, and functional versatility of organic moieties.

The synergy between organic and inorganic domains enables the engineering of multifunctional materials whose combined properties exceed those of their individual constituents.[5] For instance, the structural versatility of hybrid materials allows for the enhancement of energy conversion efficiencies in third-generation solar cells and light-emitting diodes (LEDs), contributing to improved performance and longevity.[6–8] In the realm of energy storage, hybrid materials have shown promise in reinforcing the capacity and durability of battery and supercapacitor electrodes.[9–11] Furthermore, they are widely applied in smart coatings, offering attributes such as UV resistance, anti-corrosion, and anti-fouling properties.[12,13] In catalysis, these materials act as highly efficient catalysts, particularly in photocatalytic processes for pollutant degradation and hydrogen generation.[14,15]

Various synthesis methods, including sol–gel processing, precipitation techniques, and slow evaporation, are employed to fabricate hybrid systems, each offering distinct advantages in controlling morphology, particle size, and component dispersion.[16–18] Phase transitions in these materials are often governed by intricate mechanisms, such as atomic rearrangements, modifications in intermolecular forces, or changes in lattice structure.[19] Due to the flexible nature of organic subunits and the nanoscale dimension of inorganic clusters, these transitions can exhibit behaviors not observed in homogeneous systems. Understanding and manipulating such transitions is crucial for tailoring material properties to suit specific functional applications.[20] Despite notable progress, several challenges remain in the practical development of hybrid materials,

[a]*Laboratory for Spectroscopic Characterization and Optics of Materials, Faculty of Sciences, University of Sfax, B. P. 1171, 3000 Sfax, Tunisia. E-mail: oueslatiabderrazek@yahoo.fr*

[b]*Departement of Physics, Faculty of Science, Al-Baha University, Alaqiq, 65779, Saudi Arabia*

including ensuring long-term stability, reducing production costs, and managing interfacial compatibility. Future studies are expected to focus on resolving these issues through advanced synthesis strategies and deeper insights into nanoscale interactions.

Hybrid materials incorporating antimony present particularly interesting opportunities across various high-tech domains. Thanks to their exceptional optical and electronic properties, Sb-based hybrids show great promise in applications such as waveguides, modulators, and energy storage systems. In batteries and supercapacitors, they contribute to enhanced electrode performance.[21,22] They are also good candidates for catalytic and photocatalytic applications due to their potent absorption and effective charge separation capabilities.[23] Antimony-containing perovskites, as $(CH_3NH_3)_3Sb_2I_9$, are being investigated in solar technologies to increase thermal stability and conversion efficiency.[24] Sb-based hybrids are positioned as essential materials for next-generation technologies because of their multifunctional properties. In this context, the present work investigates the antimony-based hybrid compound $[(CH_3)_4P]_3Sb_2Br_9$, with a particular focus on elucidating the origin of its phase transitions through synthesis, temperature-dependent vibrational analysis, and electrical characterization by impedance spectroscopy.

2. Experimental section

2.1. Reagents

The chemical reagents ($[(CH_3)_4P]Br$ and Sb_2O_3) were all of analytical quality and were used without any additional processing and purification.

2.2. $[(CH_3)_4P]_3Sb_2Br_9$ crystal growth

Single crystals of $[(CH_3)_4P]_3Sb_2Br_9$ were synthesized by the method of solvent evaporation under constant temperature. A concentrated aqueous solution of hydrobromic acid in water was reacted with tetramethylphosphonium bromide ($[(CH_3)_4P]Br$) and Sb_2O_3. Then, the solution was stirred for a few minutes to maintain homogeneity, and slowly evaporated for 4 days at 25 °C. To facilitate visualization, representative single crystals are displayed in Fig. 1.

2.3. Physical property measurements

An X-ray Powder Diffraction (XRPD) pattern was recorded at room temperature using a PANalyticalθ/θ Bragg–Brentano Empyrean diffractometer (CuKα_{1+2} radiations) connected with the PIXcel1D detector to verify the phase purity of the as-prepared powder. The diffraction data were collected over the 5°–100° 2θ range with a step size of 0.0131° and an acquisition time of 3 seconds per step, ensuring high counting statistics and optimal resolution. The diffraction pattern was refined using the Le Bail method[25] implemented in the FullProf program to confirm the crystallographic parameters and phase purity of the compound.[26]

To analyze the intermolecular interactions in the crystal, Hirshfeld surface analysis serves as an effective approach.[27] This technique, applied using the Crystal Explorer software,[28] separates the crystal's electron density into molecular fragments, allowing detailed investigation of how molecules are packed within the structure. The Hirshfeld surface itself is defined using two key metrics: d_e, denoting the distance from a given surface point to the closest atom outside the molecule, and d_i, representing the distance to the nearest atom inside the molecule.

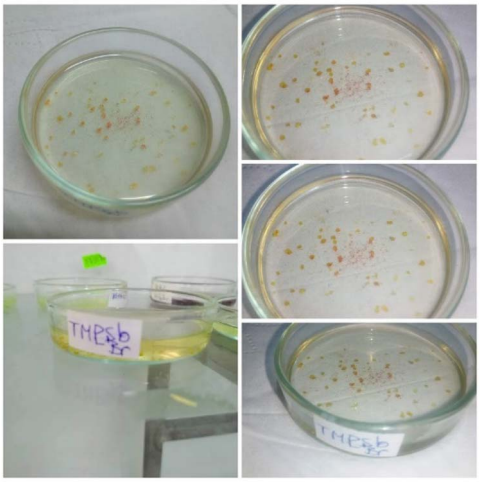

Fig. 1 The $[(CH_3)_4P]_3Sb_2Br_9$ crystals obtained by slow evaporation.

A normalized contact measure, d_{norm}, is calculated from these distances combined with atomic van der Waals radii, ensuring accurate mapping of intermolecular contacts. For visualization, d_{norm} values are color-coded: red areas show close contacts (short intermolecular distances, negative d_{norm}), white areas represent contacts at van der Waals distances (zero d_{norm}), and blue areas indicate longer contacts (positive d_{norm}). The d_{norm} mapping, generated in Crystal Explorer, enables the creation of two-dimensional fingerprint plots that summarize and classify the types of intermolecular interactions present in the crystal. In this process, the van der Waals radii for atoms (r^{vdW}) are accounted for, and the proximity of atoms internal (d_i) and external (d_e) to the surface is used to characterize specific crystal contact.

The infrared spectrum of $[(CH_3)_4P]_3Sb_2Br_9$ was acquired at room temperature in the frequency range of 500–4000 cm^{-1} using a PerkinElmer FT-IR 1000 spectrophotometer.

The Raman spectra were acquired between 70 and 3100 cm^{-1} throughout the temperature range of 294–563 K using a T64000 (Jobin-Yvon, Horiba group, Kyoto, Japan) spectrometer. An argon–krypton ion laser (Innova, Coherent, France) provided the incident wavelength light, which was then focused at 647.1 nm using an MSPlan 50× (N.A. 0.55), on an Olympus BX41 microscope. The laser power used on the sample during the experiment was less than 2 mW, and two scans of the Raman spectra were produced with an integration time of 60 seconds per scan. Then, a nitrogen-cooled, front-illuminated charge-coupled device (CCD) detector connected to a spectrometer with a single monochromator (600 gratings per millimeter) was

used to analyze the scattered light. The spectral profiles were deconvoluted using the LabSpec software with a combination of Gaussian and Lorentzian functions to enable a quantitative analysis of band evolution with temperature.

Impedance spectroscopy (IS) was employed to investigate the electrical properties of $[(CH_3)_4P]_3Sb_2Br_9$ polycrystalline powder. This technique is widely recognized for its ability to provide detailed insights into the electrical behavior of materials and their interfaces across a broad range of frequencies and temperatures.[29] In this study, the polycrystalline powder was compressed into disc-shaped pellets (8 mm diameter, 1.2 mm thickness) under uniaxial pressure of 3 t cm^{-2}. To ensure optimal electrical contact and minimize interfacial resistance, silver conductive paste was applied to both flat surfaces of each pellet before impedance measurements. Electrodes were then affixed to the silvered faces, allowing for consistent electrical connections throughout the measurement range. The pellet and its electrodes were placed between the two contacts of the Solartron SI 1260 impedance analyzer inside a temperature-controlled chamber to allow for the acquisition of impedance spectra between 433 K and 563 K.

3. Results and discussion

3.1. Structural studies

M. Wojtas' *et al.*[30] have previously published the crystal structure of $[(CH_3)_4P]_3[Sb_2Br_9]$. To complement the explanation of the physical qualities, a synopsis of its primary structural characteristics is given below for completeness.

The compound crystallizes in the trigonal system and is made up of several $[Sb_2Br_9]^{3-}$ anions and tetramethylphosphonium cations (Fig. 2). Each anion is composed of two corner-sharing $SbBr_6$ octahedra that form a bioctahedral $[Sb_2Br_9]^{3-}$ unit. With two various types of Sb–Br connections, the antimony atoms take on some form of distorted octahedral coordination: bridging bonds around 3.03 Å and terminal bonds between 2.64 and 2.80 Å (Table S1). With bond angles ranging from 91.9° to 93.2°, the Br–Sb–Br exhibits a minor departure from ideal octahedral symmetry. The geometry found in similar compounds like $[(CH_3)_4N]_3[Sb_2Br_9]$ and $[(CH_3)_4N]_3[Sb_2Br_3Cl_6]$ is compatible with the Sb···Sb separation located within the anionic dimer, which is 3.933 Å.

Weak C–H···Br hydrogen bonds between the methyl groups of the cations and the terminal bromine atoms of the anions control the crystal packing, resulting in a three-dimensional supramolecular network. *Via* local polarization effects, these interactions maintain the crystal structure and might have a little impact on the electrical and dielectric responses.

Therefore, although the crystal structure has been previously described, this detailed recall is essential to understand how the local geometry and supramolecular interactions impact the macroscopic electrical behavior of the compound studied in this work.

In order to verify the formation and purity of the synthesized compound, X-ray powder diffraction (XRPD) measurements were carried out on the obtained powder sample.

Fig. 3 shows the experimental XRPD pattern and its refinement by the Lebai method at room temperature of the $[(CH_3)P]_3Sb_2Br_9$ sample. The product is extremely pure and crystalline, as evidenced by the absence of peaks from other contaminants. Every measured line has an exact index with the predicted space group ($P3_1c$). The calculated and experimental spectra exhibit good agreement, with $\chi^2 = 17.1$, $R_p = 7.45$, $R_{wp} = 8.77$, and $R_{exp} = 2.12$, indicating a high level of refinement. The obtained unit-cell parameters are reported $a = b = 9.797(32)$ Å, $c = 22.653(90)$ Å, $\alpha = \beta = 90°$ and $\gamma = 120°$. These parameters and the experimental powder diffraction pattern matches well with the simulated pattern derived from the single crystal data.[32]

3.2. Hirshfeld surface analysis

Alongside the crystallographic study of $[(CH_3)_4P]_3Sb_2Br_9$, an in-depth investigation of intermolecular contacts was performed using Hirshfeld surface and fingerprint plot analyses. These analyses relied on the crystal structure's CIF file[30] and were

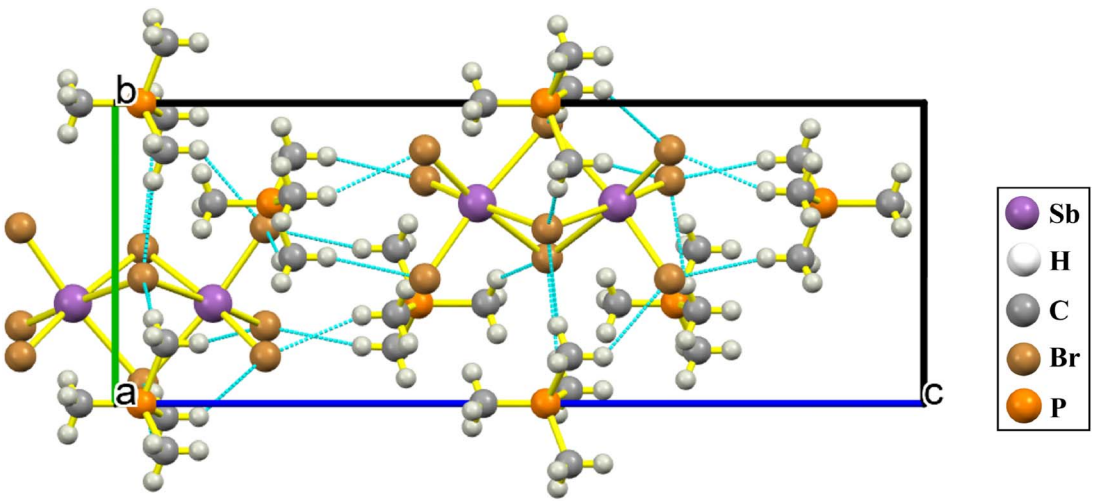

Fig. 2 Crystal structure of $[(CH_3)_4P]_3Sb_2Br_9$ viewed along the *a*-axis, generated using MERCURY software.[31]

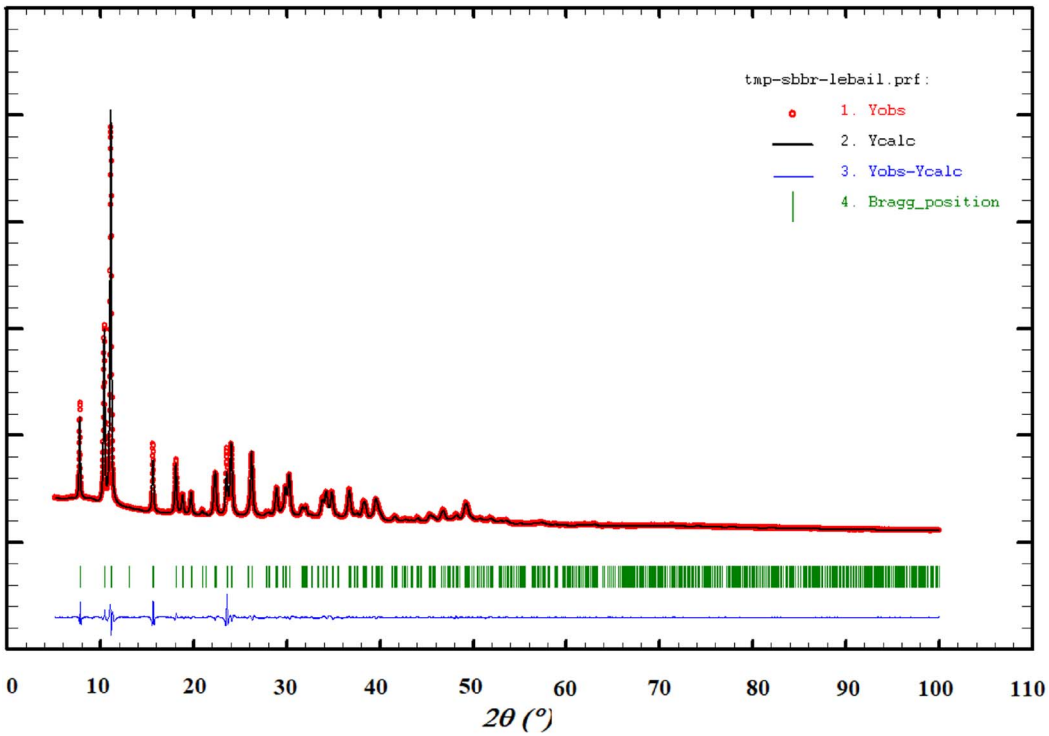

Fig. 3 Analysis of the diffraction pattern for the compound $[(CH_3)_4P]_3Sb_2Br_9$ using the Lebail method and comparing the results (black lines) with the observed patterns (red dots). Bragg peak positions of space group $P3_1c$ are shown by vertical markers.

carried out with the Crystal Explorer software, facilitating a detailed assessment of weak interactions on the molecular surface.

To delineate the specific region occupied by each molecule within the crystal, the Hirshfeld surface approach was utilized, segmenting the electron density into molecular fragments. The three-dimensional surface was mapped across several shape metrics, including d_{norm}, shape index, d_i, and d_e. As revealed in Fig. 4, mapping over d_{norm} generates three main color-coded zones: white indicates contacts matching the sum of van der Waals radii, blue suggests longer contacts, and red corresponds to closer, higher-density regions. Red patches on the d_{norm} surface point to strong interactions, such as N–H···Cl hydrogen bonds, which mark the shortest intermolecular contacts in this structure. Additionally, visualization by shape index highlights donors and acceptors involved in bonding, showing up as red, orange, or blue features near specific atoms.

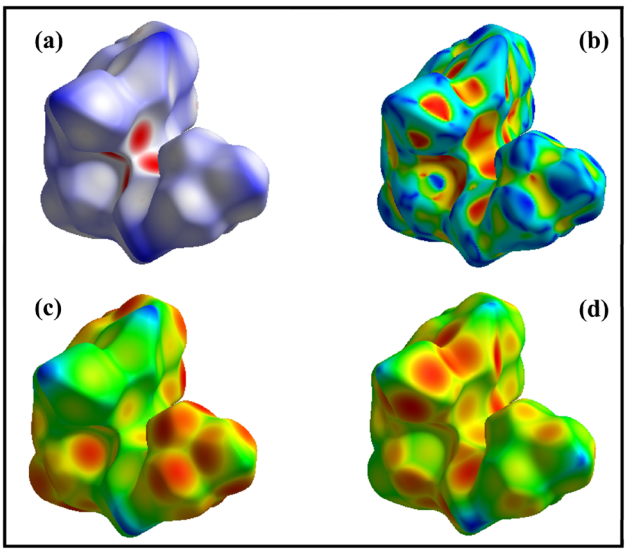

Fig. 4 Hirshfeld surfaces mapped with (a) d_{norm}, (b) shape index, (c) d_i, and (d) d_e surface for the title compound.

Analysis of the two-dimensional fingerprint plots (see Fig. 5) provided a quantitative breakdown of surface contacts: Br···H interactions accounted for 62.2% of the Hirshfeld surface, making them the main contributor to molecular packing. H···H contacts followed at 33%, reflecting the high number of surface hydrogens present. Sb···Br (3.6%), Br···Br (0.6%), and Sb···H (0.4%) contacts made smaller but measurable contributions. These findings highlight that Br···H and H···H interactions are dominant in dictating the crystal packing arrangement.

3.3. Vibrational studies

To elucidate the phase transition, Raman spectroscopy was performed in the 293–398 K range (Fig. 6), providing direct insight into lattice dynamics and cation–framework coupling. For clarity, the temperature-dependent Raman spectra are presented in three distinct wavenumber regions: 70–450 cm^{-1} (Fig. 6a), 500–1700 cm^{-1} (Fig. 6b), and 2700–3100 cm^{-1} (Fig. 6c). Complementary infrared spectra (Fig. 7) were also recorded, as the reliable assignment of Raman- and IR-active modes at room temperature is essential for interpreting temperature-induced

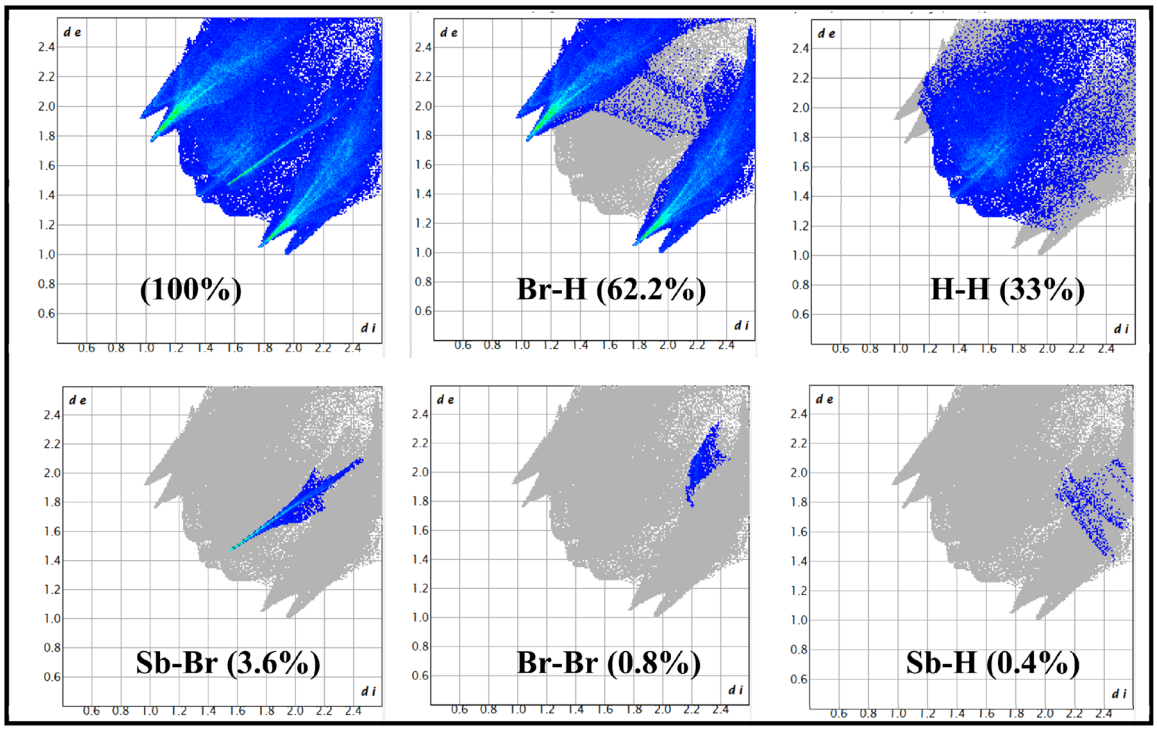

Fig. 5 2D fingerprint plots of the title compound.

structural modifications. The vibrational mode assignment at room temperature (Table 1) was established by a detailed comparison of the present spectra with those of structurally related compounds previously reported in the literature.[33–36]

In the low-frequency region below 400 cm^{-1}, the spectra are primarily characterized by lattice vibrations and internal modes of the $[Sb_2Br_9]^{3-}$ anionic unit. Above 400 cm^{-1}, the vibrational features are dominated by the $[(CH_3)_4P]^+$ cations, including

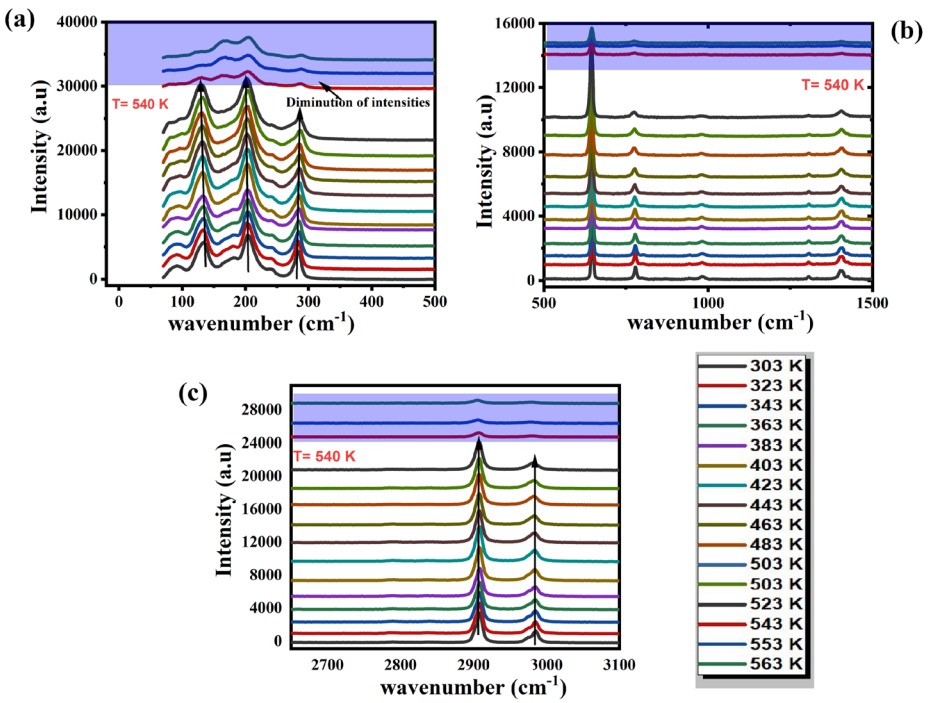

Fig. 6 Temperature evolution of the Raman spectra of $[(CH_3)_4P]_3Sb_2Br_9$ compound in the temperature range 303–563 K for selected spectral ranges (a) [70–500 cm^{-1}], (b) [500–1500 cm^{-1}], and (c) [2650–3150 cm^{-1}].

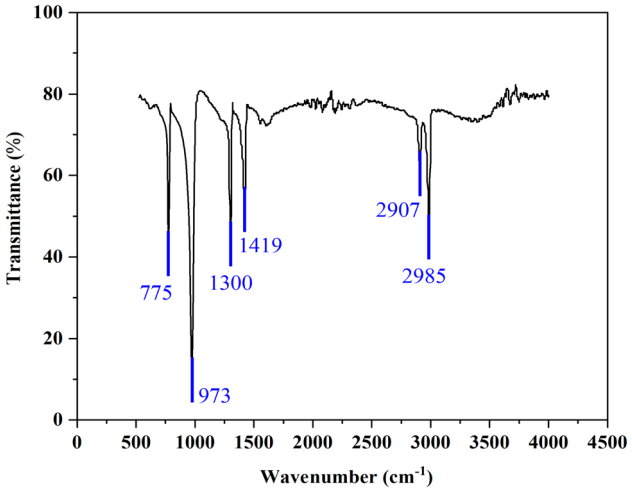

Fig. 7 Experimental IR spectrum of $[(CH_3)_4P]_3Sb_2Br_9$ at room temperature.

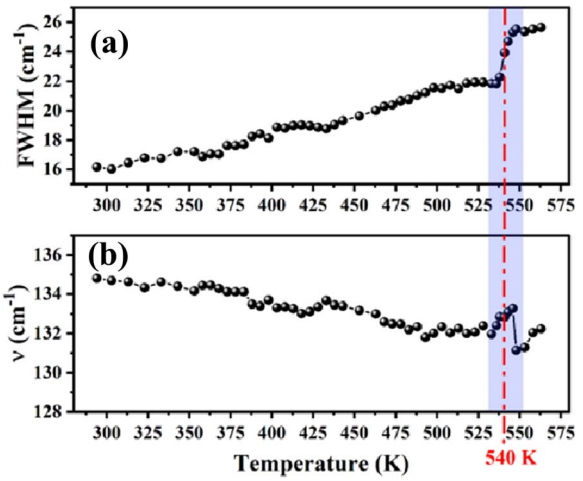

Fig. 8 Raman wavenumber temperature evolution of (a) the full width at half maximum (FWHM) of the Raman bands and (b) the position of the bands in the frequency range corresponding to δ(Sb–Br).

stretching and deformation modes of the PC_4 and CH_3 groups.[36] The high-frequency region is associated with C–H stretching vibrations from the methyl groups. All specific mode assignments and corresponding frequencies are summarized in Table 1.

Differential scanning calorimetry (DSC) measurements reported in the literature[30] reveal that $[(CH_3)_4P]_3Sb_2Br_9$ undergoes two reversible phase transitions at 193 K and 540 K upon heating. To investigate the structural dynamics underlying the high-temperature transition, a series of fifty Raman spectra was recorded between 303 K and 563 K. This temperature-dependent study provides a direct probe of molecular reorientations in both the organic cations and inorganic anions. Careful analysis of the evolving vibrational bands allows the identification of specific lattice distortions and cationic motions that accompany the phase transition, offering a detailed understanding of the mechanisms driving the structural change. The temperature dependence of the main vibrational modes, including both peak positions and full widths at half maximum (FWHM), is presented in Fig. 8–12.

Significant spectral changes are observed in the internal modes of the $[Sb_2Br_9]^{3-}$ anion. The Sb–Br bending vibration at 134 cm^{-1} exhibits a slight blue shift of less than 2 cm^{-1} accompanied by a noticeable broadening of approximately 4 cm^{-1} above 540 K. The symmetric Sb–Br stretching mode at 205 cm^{-1} shifts upward by 3 cm^{-1} and broadens to roughly 10 cm^{-1} near the transition, while the asymmetric Sb–Br stretching mode undergoes a similar broadening.

Vibrational modes associated with the tetramethylphosphonium cation are also affected by the transition. The symmetric and asymmetric PC_4 stretching vibrations at 648 and 779 cm^{-1} shift by about 1 cm^{-1} toward higher frequencies, with the asymmetric mode showing a pronounced broadening of approximately 11 cm^{-1}. The CH_3 deformation modes at 1402 and 1409 cm^{-1} merge into a single, broader band with a widening of around 6 cm^{-1} as the temperature approaches

Table 1 Raman and IR frequencies of the compound $[(CH_3)_4N]_3Sb_2Br_9$ observed at room temperature in $(cm^{-1})^a$

IR (cm^{-1})	Raman (cm^{-1})	Assignments	References	Compound
	91m	δ(Sb–Br)	35 and 37	$Cs_3Sb_2Br_9$ $(CH_3NH_3)_3Sb_2Br_9$
	133s	δ(Sb–Br)		
	181m	δ(Br–Sb–Br)		
	204s	υ(Sb–Br)		
	240m	υ(Sb–Br)		
	283s	υ(Sb–Br)		
	648s	$\upsilon_s(PC_4)$	33 and 36	$[(CH3)_4P]_3Bi_2Cl_9$ $[(CH_3)_4P]_3Sb_2Cl_9$
775m	778m	$\upsilon_{as}(PC_4)$		
973s	943w, 981w	$\rho(CH_3)$		
1300m	1305w	$\delta_s(CH_3)$		
1419m	1402m, 1408m, 1424w	$\delta_{as}(CH_3)$		
	2787w	υ(CH)	33 and 36	$[(CH3)_4P]_3Bi_2Cl_9$ $[(CH_3)_4P]_3Sb_2Cl_9$
	2840w	υ(CH)		
2907w	2909s	$\upsilon_s(CH_3)$		
2985s	2975m, 2986m	$\upsilon_{as}(CH_3)$		

[a] W: weak; m: medium; s: strong.

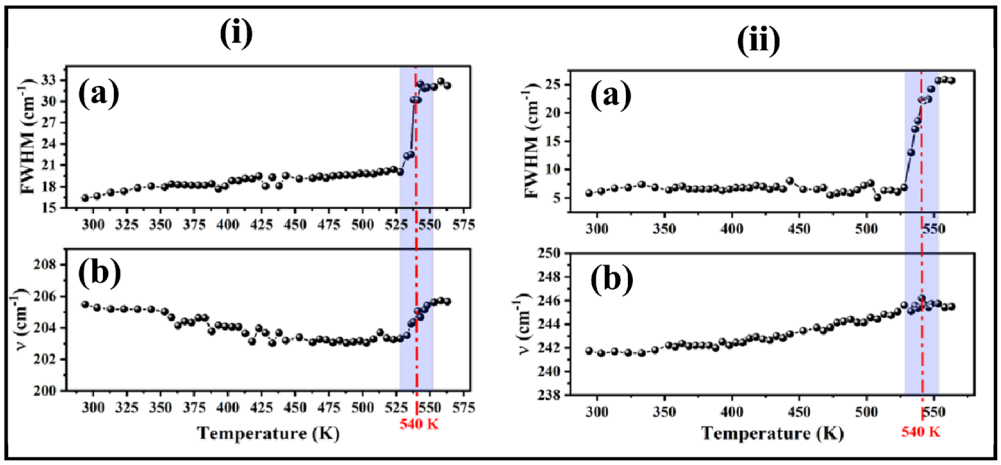

Fig. 9 (i) Raman wavenumber temperature evolution of (a) the full width at half maximum (FWHM) of the Raman bands and (b) the position of the bands in the frequency range corresponding to ν_a(Sb–Br). (ii) Raman wavenumber temperature evolution of (a) the full width at half maximum (FWHM) of the Raman bands and (b) the position of the bands in the frequency range corresponding to ν_{as}(Sb–Br).

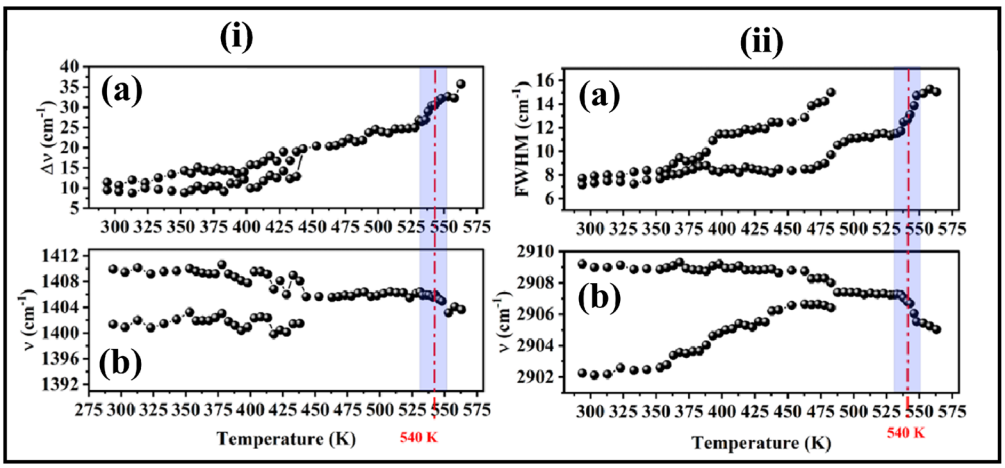

Fig. 10 (i) Raman wavenumber temperature evolution of (a) the full width at half maximum (FWHM) of the Raman bands and (b) the position of the bands in the frequency range corresponding to $\nu_{as}(CH_3)$. (ii) Raman wavenumber temperature evolution of (a) the full width at half maximum (FWHM) of the Raman bands and (b) the position of the bands in the frequency range corresponding to $\nu_s(CH_3)$.

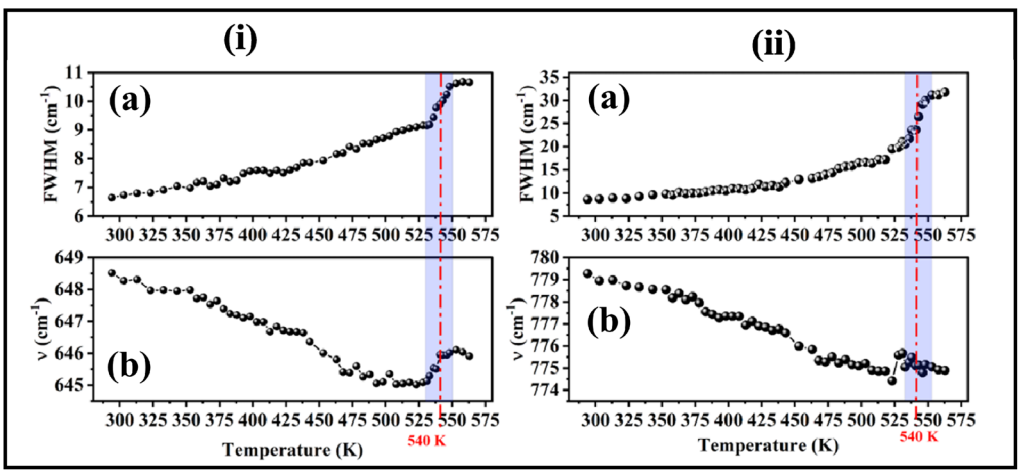

Fig. 11 (i) Raman wavenumber temperature evolution of (a) the full width at half maximum (FWHM) of the Raman bands and (b) the position of the bands in the frequency range corresponding to $\nu_a(PC_4)$. (ii) Raman wavenumber temperature evolution of (a) the full width at half maximum (FWHM) of the Raman bands and (b) the position of the bands in the frequency range corresponding to $\nu_{as}(PC_4)$.

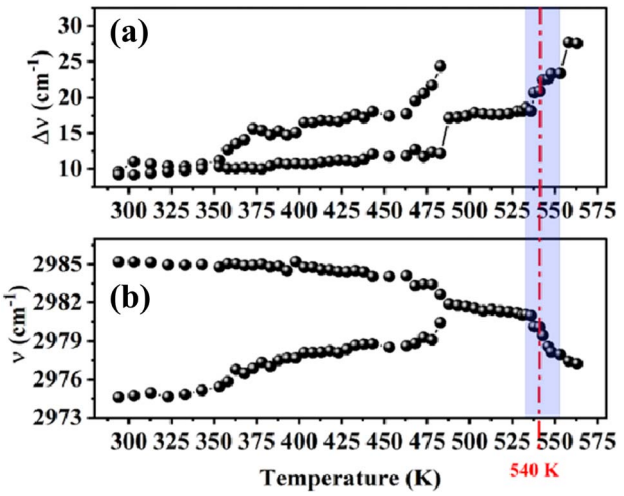

Fig. 12 Raman wavenumber temperature evolution of (a) the full width at half maximum (FWHM) of the Raman bands and (b) the position of the bands in the frequency range corresponding to $\delta(CH_3)$.

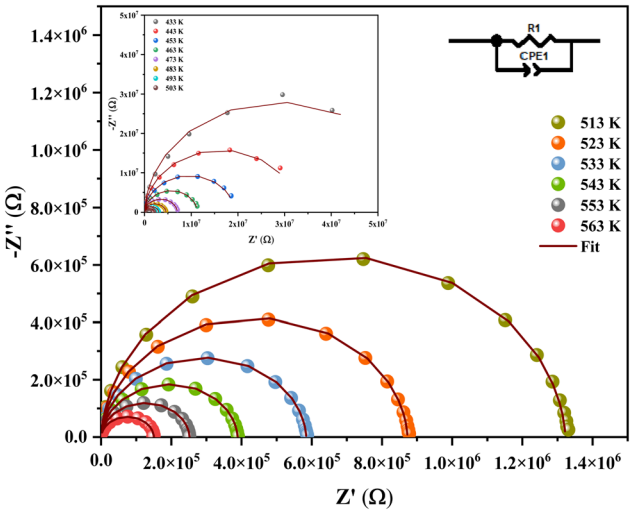

Fig. 13 Nyquist plots of $[(CH_3)_4P]_3Sb_2Br_9$ at different temperatures. The inset shows a representative Nyquist plot recorded in a temperature range [433–503 K], together with the equivalent circuit used for fitting the experimental data.

540 K. Similarly, the symmetric CH_3 stretching mode between 2902 and 2909 cm^{-1} shifts by 4 cm^{-1}, and the asymmetric CH_3 stretching modes at 2974 and 2975 cm^{-1} coalesce into a single peak with an increase in FWHM of about 5 cm^{-1} above 540 K.

These observations highlight the active participation of both cationic and anionic substructures in the phase transition. The abrupt changes in peak positions and spectral widths, particularly beyond 540 K, indicate the onset of a disordered phase consistent with an order–disorder transition mechanism. Most vibrational modes display discontinuities at the transition, further supporting this interpretation.

The electric response of $[(CH_3)_4P]_3Sb_2Br_9$ will be significantly impacted by the fact that temperature-driven structural dynamics, molecular vibrational, and lattice scatter occur at 540 K, according to Raman spectroscopy results. Impedance spectroscopy and dielectric measurements were carried out across a wide temperature range to investigate these effects. The rivalry between the structural dynamism processes and the charge transport in the compound is fully described, and correlations between vibrational changes and the evolution of electrical conduction and dielectric characteristics are made possible.

3.4. Complex impedance measurements results

The Nyquist plots of $[(CH_3)_4P]_3Sb_2Br_9$ under study at temperatures between 433 and 563 K are displayed in Fig. 13. The overall impedance of a polycrystalline sample is determined by the interfaces between neighboring grains as well as the grains themselves, which are the highly conductive cores of the material. Depending on the relative levels of the conductivity in the two regions, one or two arcs may be seen in the Nyquist plot; generally, the conductivity of the grain interiors is higher than that of the grain borders.

The time constants for grain conductivity and grain boundaries need to differ greatly for two distinct arcs to form. There are two situations in which a single arc may be seen in the Nyquist plot: (a) if the grain boundaries are highly conductive, meaning that they efficiently transmit charge without a significant impedance, they may not form a distinct arc; and (b) if the bulk conductivity is very high, the grain arc associated with grain conductivity is so small as to be imperceptible, and only the contribution from grain boundaries is observed.

At every temperature examined, the chemical under study exhibits a single depressed semicircular arc in its spectra. The observation of only one arc must be interpreted by hypothesis (b) above, because the impedance of the grain borders is crucial in this scenario, implying that the arcs seen in the Nyquist plots represent the behavior of the sample's grain boundaries. The hypothesized electrode-material interface contribution to the observed impedance is not present for the sample under study. Conversely, the fact that the measured arc radii decrease with temperature suggests that the material under study contains thermally active relaxation processes. Moreover, each arc's center is below the Z'-axis, indicating that the material does not behave in a Debye-type manner.[38]

The measured impedance data were fitted using the *Z*-view program to a typical equivalent circuit made up of two parallel elements: a fractal capacity element (also known as a constant phase element or CPE_1) and a resistance element R_1 (see insert in Fig. 13). In the equivalent circuit, the non-ideal capacitance behavior of the material is compensated for by the CPE element ($Z_{CPE1} = 1/Q_1(j\omega)^{\alpha_1}$, where j is the imaginary number, w the angular frequency, and α_1 a constant whose value stays between 0 and 1, being zero for the pure resistive behavior and unity for the pure capacitive behavior[39]). The data in Fig. 13 makes it abundantly evident that the equivalent circuit model accurately reproduces the experimental data. Table 2 shows the corresponding circuit characteristics.

Fig. 14(a and b) illustrates the behavior of the real (Z') and imaginary (Z'') components of the complex impedance as a function of frequency at various temperatures.

Table 2 Electrical fitted circuit parameters for $[(CH_3)_4P]_3Sb_2Br_9$ at different temperatures

T (K)	α_1	Q_1 ($\times 10^{-11}$ F)	R_1 ($\times 10^5$ Ω)
433	0.97722	4.71	578
443	0.97537	4.84	327
453	0.97377	4.98	193
463	0.97399	5.01	114
473	0.97299	5.10	70.3
483	0.97195	5.20	45.7
493	0.9714	5.27	30.2
503	0.97089	5.33	20.1
513	0.96992	5.52	13.2
523	0.96878	5.65	8.7287
533	0.96729	5.83	5.8442
543	0.96553	6.05	3.8893
553	0.96407	6.26	2.5199
563	0.96427	6.40	1.5026

The Z' spectra (Fig. 14a) reveal two distinct regions: (i) a low-frequency plateau where Z' remains nearly constant, attributed to the long-range motion of charge carriers traversing the material, and (ii) a frequency-dependent region at intermediate frequencies, associated with AC conductivity. In this regime, AC conduction arises from localized, short-range movements of charge carriers that occur after they overcome potential barriers within the material. At lower temperatures, Z' is larger in the low-frequency range but decreases progressively with increasing temperature or frequency. This trend suggests a semiconductor-like behavior, indicating that $[(CH_3)_4P]_3Sb_2Br_9$ possesses a negative temperature coefficient of resistance (NTCR).[40] At higher frequencies, the Z' curves converge, reflecting the presence of *a* space charge region. The NTCR behavior suggests that $[(CH_3)_4P]_3Sb_2Br_9$ could serve as a thermistor material.[41]

The Z'' spectra (Fig. 14b) exhibit an initial rise with frequency, reaching a peak at the material's characteristic relaxation frequency, ω_{max} (where resistance equals reactance), followed by a decline at higher frequencies. These relaxation peaks are broad, asymmetric, and indicative of non-Debye-type relaxation behavior.[38,42] As the temperature increases, the peak height decreases while shifting towards higher frequencies, confirming thermally activated relaxation processes in $[(CH_3)_4P]_3Sb_2Br_9$ and an increase in the electron hopping rate with temperature.

At higher frequencies, polarization decreases because the reduced relaxation time of hopping electrons prevents them from keeping pace with the alternating electric field. Moreover, space charge polarization is prominent in the low-frequency range but becomes negligible at higher frequencies, as evidenced by the complete overlap of Z'' values in this region.

In this study, the experimental Z' (real part) and Z'' (imaginary part) spectra, presented in Fig. 14, were fitted using the theoretical models described by eqn (1) and (2), respectively. In Fig. 14a, the solid lines represent the fits to the Z' data using eqn (1), while in Fig. 14b, the solid lines correspond to the fits of the Z'' data using eqn (2).

$$Z' = \frac{R_1\left(R_1Q_1\omega^{\alpha_1}\cos\left(\frac{\alpha_1\pi}{2}\right)+1\right)}{\left[\left(1+R_1Q_1\omega^{\alpha_1}\cos\left(\frac{\alpha_1\pi}{2}\right)\right)^2+\left(R_1Q_1\omega^{\alpha_1}\sin\left(\frac{\alpha_1\pi}{2}\right)\right)^2\right]} \quad (1)$$

$$-Z'' = \frac{R_1Q_1\omega^{\alpha_1}\sin\left(\frac{\alpha_1\pi}{2}\right)+1}{\left[\left(1+R_1Q_1\omega^{\alpha_1}\cos\left(\frac{\alpha_1\pi}{2}\right)\right)^2+\left(R_1Q_1\omega^{\alpha_1}\sin\left(\frac{\alpha_1\pi}{2}\right)\right)^2\right]} \quad (2)$$

Here, α_1 is the fitting parameter, with values ranging from 0 to 1 for non-Debye-type relaxation, and equal to 1 for pure Debye relaxation. This parameter characterizes the material's relaxation mechanism and is linked to grain boundary contributions.[43] As shown in the inset of Fig. 14(a and b), the theoretical curves exhibit an excellent match with the experimental data, and the values of α_1 consistently fall between 0 and 1 across all temperatures (Table 2).

These results confirm that the relaxation mechanism in $[(CH_3)_4P]_3Sb_2Br_9$ is non-Debye in nature, indicating the

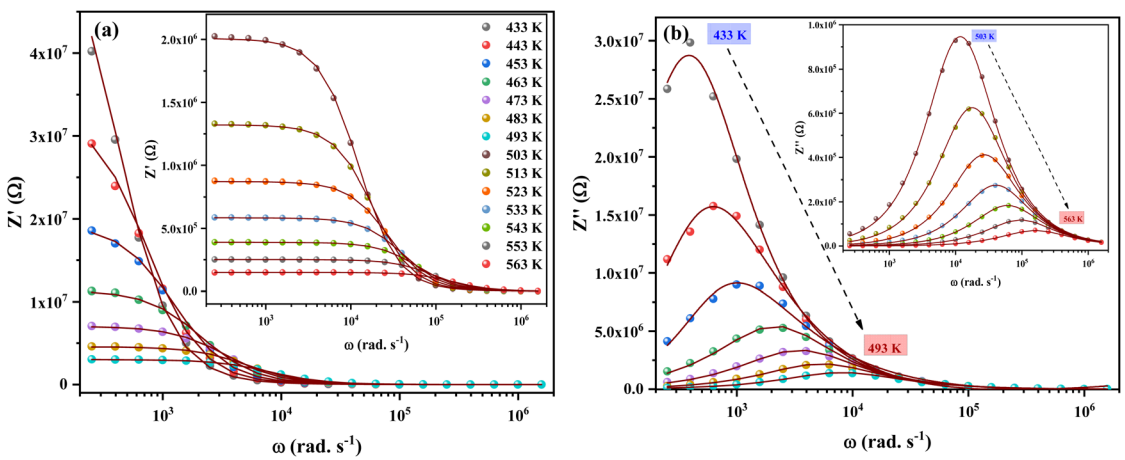

Fig. 14 (a) Temperature and frequency dependence of the real component of impedance variation. (b) Temperature and frequency dependence of the imaginary component of impedance variation. Fits shown as line plots represent the results of eqn (1) and (2) for Z' and Z'', respectively.

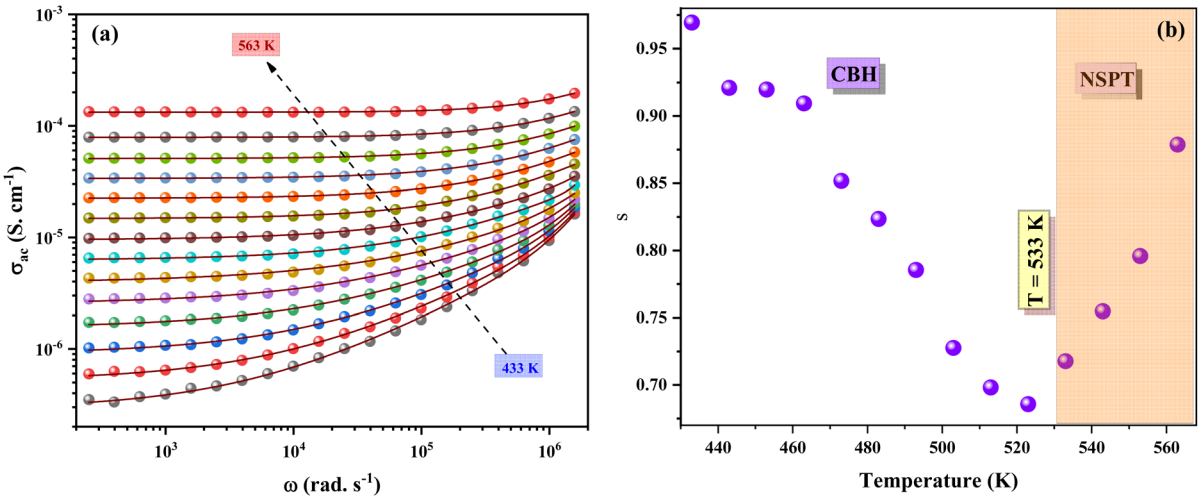

Fig. 15 (a) Variation of the ac electrical conductivity *vs.* the frequency at different temperatures. (b) Variation of the parameter s as a function of temperature. "CBH" refers to the Correlated Barrier Hopping mechanism, while "NSPT" stands for Non-Stationary Polaron Transport.

Table 3 Extracted fitting parameters (σ_{dc}, A, and s) obtained from Jonscher's universal power law for AC conductivity at different temperatures

T (K)	A	σ_{dc}	s
433	6.39×10^{-11}	3.334×10^{-7}	0.969
443	1.50×10^{-11}	6.285×10^{-7}	0.920
453	5.37×10^{-12}	1.034×10^{-6}	0.919
463	1.49×10^{-12}	1.726×10^{-6}	0.909
473	1.09×10^{-12}	2.805×10^{-6}	0.851
483	9.09×10^{-13}	4.294×10^{-6}	0.823
493	4.18×10^{-13}	6.556×10^{-6}	0.785
503	2.21×10^{-13}	9.856×10^{-6}	0.727
513	8.93×10^{-14}	1.498×10^{-5}	0.698
523	6.12×10^{-14}	2.270×10^{-5}	0.685
533	3.11×10^{-14}	3.390×10^{-5}	0.717
543	1.19×10^{-14}	5.104×10^{-5}	0.754
553	1.11×10^{-14}	7.9×10^{-5}	0.795
563	1.09×10^{-16}	1.337×10^{-4}	0.878

presence of a single relaxation process over the studied frequency and temperature ranges.

3.5. Conductivity analysis

The study of electrical conductivity aimed to provide a comprehensive understanding of the material's intrinsic characteristics and their potential relevance in electronic device applications. Additionally, the investigation focused on unraveling the nature of charge carrier transport mechanisms and their interactions within the material matrix.[44] To model the behavior of AC conductivity, Jonscher proposed an empirical relationship expressed as:[45]

Here, σ_{dc} & ZeroWidthSpace; represents the dc conductivity, which is independent of frequency, while $A\omega^s$ denotes the dispersive component that varies with frequency. The parameter s is a dimensionless factor that depends on both frequency and temperature, while A is a temperature-dependent constant. According to Jonscher's theory, the relaxation dynamics of mobile charge carriers contribute significantly to the observed AC conductivity. When these carriers move between two potential energy minima, their motion can be categorized as translational ($s < 1$), indicative of extended charge transport, or localized ($s > 1$), where carriers remain confined within a restricted spatial domain.

$$\sigma_{ac} = \sigma_{dc} + A\omega^s \quad (3)$$

At elevated temperatures, the ac conductivity spectra reveal two distinct regions. In the low-frequency domain, a plateau emerges where conductivity remains nearly independent of frequency. This region is associated with the long-range translational motion of charge carriers,[46] as shown in Fig. 15a. In contrast, at higher frequencies, the conductivity increases following a power-law dependence on ω^s. The transition frequency, marking the crossover between dc-dominated and dispersive regimes, shifts toward higher frequencies with increasing temperature. This behavior reflects the enhanced mobility of charge carriers at elevated thermal energies, facilitating more rapid hopping or tunneling processes over shorter length scales. Such temperature-dependent shifting of the crossover frequency indicates a thermally activated conduction mechanism, consistent with models based on correlated barrier hopping or quantum mechanical tunneling.

To ensure the reliability of the proposed conduction mechanisms, the experimental conductivity spectra were systematically fitted using Jonscher's universal power law. The fitting, presented in Fig. 15b, closely reproduces the experimental data, thereby confirming the adequacy of the model in describing the AC response of the studied material. The extracted parameters, including σ_{dc}, A, and s across different temperatures, are listed in Table 3.

These results not only validate the theoretical framework but also provide quantitative evidence for the evolution of charge transport processes with temperature.

The temperature-dependent behavior of the parameter *s* provides critical insights into the nature of charge hopping and transport mechanisms in the material. As reported in the literature, *s* exhibit distinct variations depending on the underlying physical processes and charge carrier type (*e.g.*, atoms, electrons, polarons). These mechanisms include:[47–50]

- Quantum mechanical tunneling (QMT): In this model, the exponent *s* is approximately 0.8 and either remains constant or shows a slight increase with temperature.
- Correlated barrier hopping (CBH): In this case, the exponent *s* decreases with rising temperature.
- Overlapping large-polaron tunneling (OLPT): where *s* decreases with increasing temperature to a minimum value, then rises again as the temperature increases.
- Non-overlapping small-polaron Tunneling (NSPT): In this model, *s* increases with temperature.

For the studied material, the graph in Fig. 15b reveals a discontinuity at 533 K, which corresponds to the phase transition observed in the DSC analysis.

- For the temperature range of 433 K to 533 K, the exponent *s* decreases as the temperature rises. This trend aligns closely with the CBH mechanism, suggesting that charge carriers hop between localized states separated by correlated potential barriers.

As the temperature increases, the thermal energy enables carriers to overcome these barriers more easily, resulting in enhanced hopping conductivity and a corresponding reduction in *s*. This behavior reflects a thermally activated transport process.

- For the temperature range of 533 K to 563 K, the (NSPT) model is shown to be appropriate since the exponents increase with increasing temperature.

Overall, the combined analysis of *s* across the phase transition provides valuable insight into the evolution of charge transport mechanisms: from hopping conduction governed by correlated barriers in the low-temperature phase, to polaronic tunneling influenced by lattice modifications in the high-temperature phase. This understanding is crucial for tailoring material properties to meet the requirements of applications that rely on temperature-dependent electrical conductivity.

3.6. Electric modulus

The variation of the real part of the complex modulus (M') as a function of frequency at different temperatures is displayed in Fig. 16a. At low frequencies, M' approaches zero for all temperatures studied. This behavior can be explained by the dominance of the long-range motion of charge carriers, which enables effective charge transport across the material without significant resistance. Additionally, the low-frequency region is unaffected by electrode polarization effects, which are often observed in impedance measurements and can obscure intrinsic material properties.[38] As the frequency increases, M' begins to rise monotonically. This increase is attributed to the short-range mobility of charge carriers, where their movement is restricted to localized hopping within the material's structure.[51] This shift indicates a frequency-dependent transition in the conduction mechanism from long-range transport to localized dynamics.

Fig. 16b illustrates the frequency-dependent behavior of the imaginary part of the complex modulus (M''). In the low-frequency region, no M'' peaks are observed, indicating that charge carriers can hop effectively between sites without significant energy barriers. This is consistent with long-range charge transport, where carriers experience minimal impedance. However, at higher frequencies, a pronounced M'' peak emerges. This peak corresponds to the transition of charge carriers from long-range translational motion to localized motion within their potential energy wells. At these frequencies, charge carriers become confined and can only oscillate locally within the bounds of their energy barriers, reflecting a short-range transport mechanism.[52]

The position of the M'' peak shifts to higher frequencies with increasing temperature, signifying thermally activated

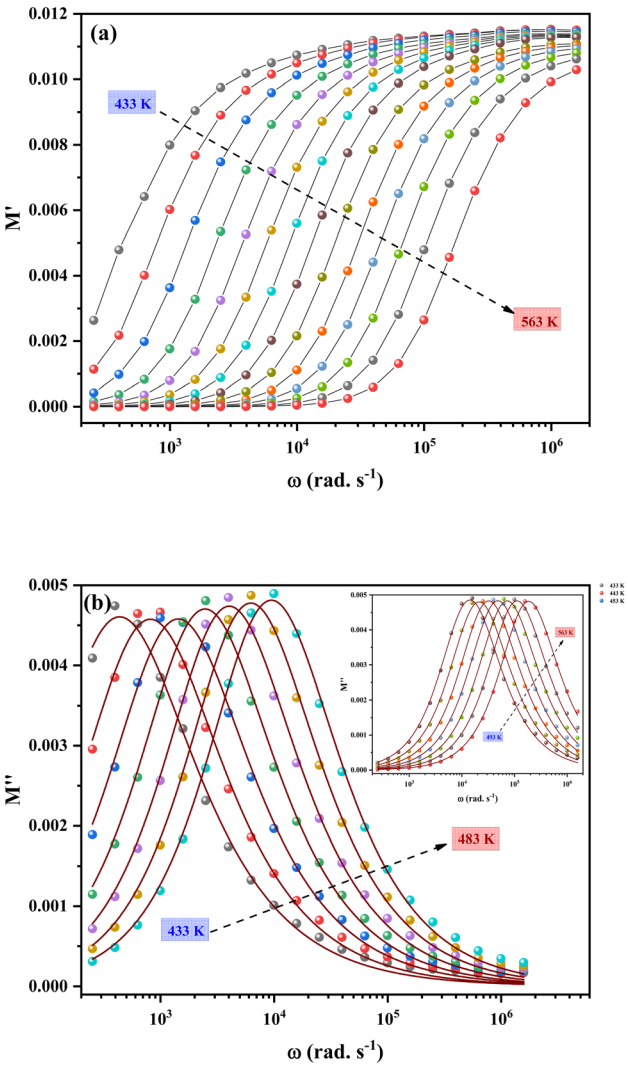

Fig. 16 (a) Frequency dependence of M' at different temperatures of $[(CH_3)_4P]_3Sb_2Br_9$. (b) Frequency dependence of M'' at different temperatures of $[(CH_3)_4P]_3Sb_2Br_9$. The peak is fitted using the model described by eqn (4).

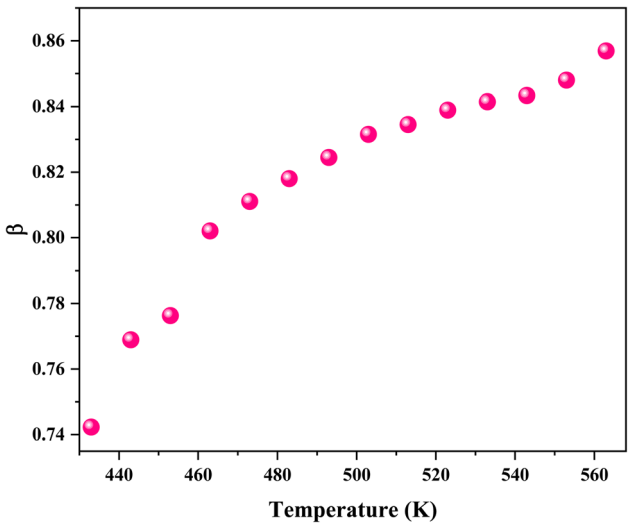

Fig. 17 Variation of the constant β as a function of temperature.

dielectric relaxation. This behavior indicates that as the temperature rises, the charge carriers gain sufficient thermal energy to overcome energy barriers more rapidly, thereby increasing the relaxation frequency. Moreover, the asymmetric shape of the observed M'' peaks support the presence of non-Debye relaxation, which deviates from the ideal Debye model. This is a typical characteristic of materials like $[(CH_3)_4P]_3Sb_2Br_9$, where complex structural and dynamic interactions among charge carriers and the material lattice lead to a distribution of relaxation times.[53]

To further analyze the relaxation behavior, numerical simulations of the modulus spectra were performed. These simulations enable the extraction of important parameters, such as activation energy and relaxation frequency, which provide insights into the dynamics of charge carriers. Bergman's frequency-dependent representation of the Kohlrausch–Williams–Watts (KWW) function is given as:[54]

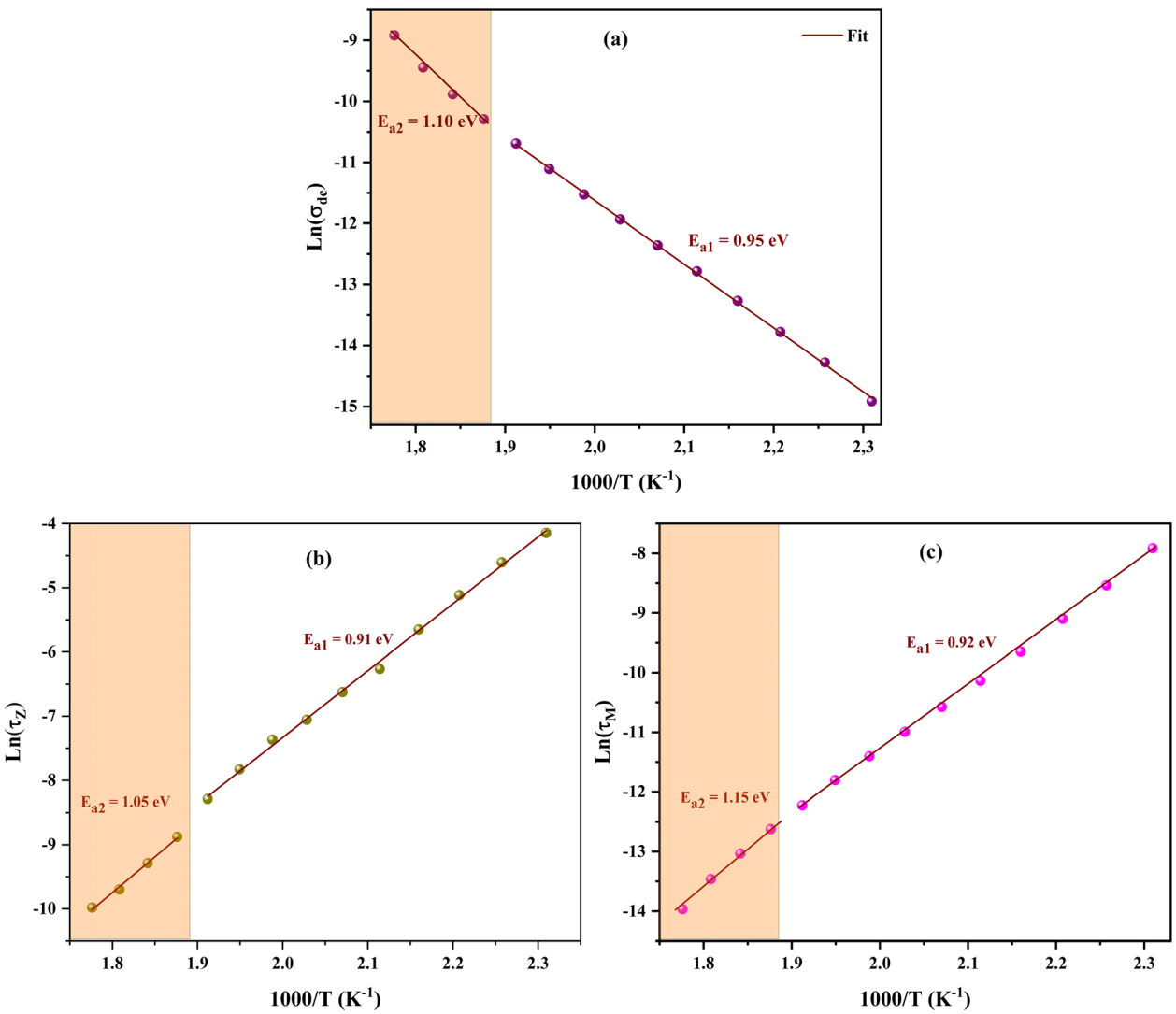

Fig. 18 Arrhenius plots constructed using (a) the σ_{dc} conductivity values, (b) the measured Z'' peak values, (c) the measured M'' peak values, at different temperatures.

$$M''(f) = \frac{M''_{max}}{\left[(1-\beta) + \left(\frac{\beta}{1+\beta}\right)\left[\beta\left(\frac{\omega_{max}}{\omega}\right) + \left(\frac{\omega_{max}}{\omega}\right)^{\beta}\right]\right]} \quad (4)$$

Here, M''_{max} represents the maximum value of the imaginary component at the corresponding angular frequency ω_{max}, while β is the Kohlrausch parameter that quantifies the degree of non-Debye behavior. The parameter β ranges between 0 and 1. In this study, the $\beta < 1$ value (Fig. 17) confirms the predominance of non-Debye relaxation.

3.7. Activation energy

The activation energy (E_a) can be determined using the Arrhenius equation derived from the dc conductivity (Fig. 18):[49]

$$\sigma_{dc} = \sigma_0 e^{-\frac{E_a}{k_B T}} \quad (5)$$

Here, k_B is the Boltzmann constant, and σ_0 is the pre-exponential factor. Using this method, two distinct regions ((1) and (2)) are identified by a change in slope at $T = 533$ K, which corresponds to the phase transition observed in the DSC analysis.[30] The activation energies calculated from the linear fits of the conductivity curve in the two regions are $E_{a1} = 0.92$ eV and $E_{a2} = 1.10$ eV, respectively.

Additional evaluations of E_a were conducted for the studied material using alternative approaches. These involve analyzing the peak values of Z'' and M'' at various temperatures. These methods yielded activation energy values of $E_{a1} = 0.91$ eV, $E_{a1} = 0.92$ eV, and $E_{a2} = 1.05$ eV and $E_{a2} = 1.15$ eV, respectively. These results closely align with the value obtained from the dc conductivity and confirm that the same underlying mechanism governs both electric conduction and dielectric polarization in the material.[38]

Several factors can affect the activation energy, with the ionic radius playing a crucial role in ionic conduction. Ions with smaller ionic radii typically move more easily compared to larger ions. Among the ions present, Sb^{3+} has the smallest ionic radius, followed by Br^-, while the $[(CH_3)_4P]^{3+}$ cation has a much larger ionic radius.[55,56]

Considering the ionic radii and electronegativities of the constituent species, the $[Sb_2Br_9]^{3-}$ anion framework provides a pathway for limited anionic motion, while the high electronegativity of Br^- restricts its mobility. Combined with the impedance and σ_{dc} results indicating ionic conduction, this suggests that H^+ is the dominant charge carrier.[38] Such protonic conduction, facilitated by hydrogen-bond networks, is well-documented in hybrid halometallates.[57,58]

These electrical results are consistent with the Raman analysis as a function of temperature. In both cases, the modifications observed near the phase transition reveal significant changes in the vibrational dynamics of the lattice, involving both the organic and inorganic sublattices, with more pronounced variations in the inorganic framework. Such coupling between structural vibrations and electrical response highlights the key role of the inorganic moieties in governing the overall behavior of the hybrid system. Such combined structural and electrical features open interesting perspectives for potential applications of this material, whether as a hybrid compound exhibiting phase transitions, as an ionic conductor, or as a functional material for energy-related technologies.

4. Conclusion

$[(CH_3)_4P]_3Sb_2Br_9$ was thoroughly investigated by combining temperature-dependent vibrational and impedance spectroscopies. The compound crystallizes in a monoclinic phase with $P3_1c$ symmetry, as proven by X-ray powder diffraction. Significant structural rearrangements and dynamic reorientations were found in both the organic and inorganic frameworks using temperature-dependent Raman spectroscopy, especially close to the reversible phase transition at about 540 ± 7 K. An order–disorder mechanism is supported by the observed shifts, widening, and coalescence of vibrational bands, which show improved molecule reorientations and lattice dynamics. Across all temperatures, impedance spectroscopy revealed a single semicircular arc, suggesting that the electrical response was mostly caused by grain-related factors. In accordance with Jonscher's power law, thermally activated conduction regulated by Correlated Barrier Hopping (CBH) and Non-overlapping Small Polaron Tunneling (NSPT) mechanisms was discovered through analysis using an equivalent circuit model and frequency-dependent conductivity measurements. These findings demonstrate that the main charge carriers in this hybrid material are H^+ ions. Given its pronounced phase transition near 540 K, efficient proton conductivity, and robust structural order, $[(CH_3)_4P]_3Sb_2Br_9$ demonstrates distinct promise for practical applications. For example, these properties make it an attractive candidate for solid-state electrolyte materials in next-generation proton-conducting fuel cells and energy storage devices, where fast and thermally activated ionic transport is required. Additionally, the combination of reversible structural phase transitions and proton conductivity could be exploited in phase-change memory devices or temperature sensors, with the material's electrical response offering a direct readout of environmental changes. Its hybrid nature and stability also suggest potential utility in optoelectronic switches, where synergistic control over electronic and structural properties is advantageous.

Author contributions

Khaoula Ben Brahim: Writing – original draft, visualization, methodology, investigation, formal analysis. Arafat Ghoudi: Writing – review & editing, software, methodology, investigation. Ines Mbarek: Writing – original draft, visualization, methodology, investigation, formal analysis. Noweir Ahmad Alghamdi: Writing – original draft, visualization, methodology, investigation, formal analysis. Malika Ben Gzaiel writing – original draft, supervision, methodology, Abderrazek Oueslati: Writing – original draft, supervision, validation, project administration.

Conflicts of interest

The authors declare that they have no known competing financial interests or personal relationships that could have appeared to influence the work reported in this paper.

Data availability

The authors confirm that the data used to support the findings of this study are included within the article and are available from the corresponding author upon reasonable request.

Supplementary information is available. See DOI: **https://doi.org/10.1039/d5ra06870c**.

References

1 S. K. Abdel-Aal, M. F. Kandeel, A. F. El-Sherif and A. S. Abdel-Rahman, Synthesis, Characterization, and Optical Properties of New Organic–Inorganic Hybrid Perovskites [(NH3)2(CH2)3]CuCl4 and [(NH3)2(CH2)4]CuCl2Br2, *Phys. Status Solidi A*, 2021, **218**(12), 2100036.

2 C. R. Bowen, R. Boomishankar, T. Vijayakanth, D. J. Liptrot and E. Gazit. Recent Advances in Organic and Organic–Inorganic Hybrid Materials for Piezoelectric Mechanical Energy Harvesting. 2022, disponible sur: **http://dr.iiserpune.ac.in:8080/xmlui/handle/123456789/6536**.

3 L. Yue, K. Yang, X. Y. Lou, Y. W. Yang and R. Wang, Versatile Roles of Macrocycles in Organic-Inorganic Hybrid Materials for Biomedical Applications, *Matter*, 2020, **3**(5), 1557–1588.

4 W. Mao, J. Wang, X. Hu, B. Zhou, G. Zheng, S. Mo, *et al.*, Synthesis, crystal structure, photoluminescence properties of organic-inorganic hybrid materials based on ethylenediamine bromide, *J. Saudi Chem. Soc.*, 2020, **24**(1), 52–60.

5 I. Garoui, M. Mallek, F. N. Almutairi, W. Rekik and A. Oueslati, Synthesis, Structural characterization and complex impedance analysis of a novel organic-inorganic hybrid compound based on Mercury (II) chloride, *J. Mol. Struct.*, 2024, **1315**, 138881.

6 Z. Zhao, F. Gu, H. Rao, S. Ye, Z. Liu, Z. Bian, *et al.*, Metal Halide Perovskite Materials for Solar Cells with Long-Term Stability, *Adv. Energy Mater.*, 2019, **9**(3), 1802671.

7 X. Tian, Y. Zhang, R. Zheng, D. Wei and J. Liu, Two-dimensional organic–inorganic hybrid Ruddlesden–Popper perovskite materials: preparation, enhanced stability, and applications in photodetection, *Sustainable Energy Fuels*, 2020, **4**(5), 2087–2113.

8 X. Zheng, Y. Deng, B. Chen, H. Wei, X. Xiao, Y. Fang, *et al.*, Dual Functions of Crystallization Control and Defect Passivation Enabled by Sulfonic Zwitterions for Stable and Efficient Perovskite Solar Cells, *Adv. Mater.*, 2018, **30**(52), 1803428.

9 M. Z. Iqbal and U. Aziz, Supercapattery: Merging of battery-supercapacitor electrodes for hybrid energy storage devices, *J. Energy Storage*, 2022, **46**, 103823.

10 K. Wang, R. Bi, M. Huang, B. Lv, H. Wang, C. Li, *et al.*, Porous Cobalt Metal–Organic Frameworks as Active Elements in Battery–Supercapacitor Hybrid Devices, *Inorg. Chem.*, 2020, **59**(10), 6808–6814.

11 N. Cheng, L. Ren, X. Xu, Y. Du and S. X. Dou, Application of organic-inorganic hybrids in lithium batteries, *Mater. Today Phys.*, 2020, **15**, 100289.

12 Z. Zhou, A. Seif, S. Pourhashem, J. Duan, A. Rashidi, M. Mirzaee, *et al.*, Anti-corrosion and anti-fouling properties of ball-like GQDs hybrided MOFs functionalized with silane in waterborne epoxy-polydimethylsiloxane coatings: Experimental and theoretical studies, *Appl. Mater. Today*, 2023, **30**, 101704.

13 F. Liu, A. Liu, W. Tao and Y. Yang, Preparation of UV curable organic/inorganic hybrid coatings-a review, *Prog. Org. Coat.*, 2020, **145**, 105685.

14 E. D. Goodman, C. Zhou and M. Cargnello, Design of Organic/Inorganic Hybrid Catalysts for Energy and Environmental Applications, *ACS Cent. Sci.*, 2020, **6**(11), 1916–1937.

15 K. R. Barnard, V. R. Bright, R. J. Enright, K. M. Fahy, A. C. Liu and P. E. Hoggard, Heterogeneous Catalysis by Tetraethylammonium Tetrachloroferrate of the Photooxidation of Toluene by Visible and Near-UV Light, *Catalysts*, 2018, **8**(2), 79.

16 F. X. Perrin, F. Ziarelli and A. Dupuis, Relation between the corrosion resistance and the chemical structure of hybrid sol-gel coatings with interlinked inorganic-organic network, *Prog. Org. Coat.*, 2020, **141**, 105532.

17 N. Ahadi, M. A. Bodaghifard and A. Mobinikhaledi, Preparation and characterization of a novel organic–inorganic hybrid nanostructure: application in synthesis of spirocompounds, *Res. Chem. Intermed.*, 2020, **46**(7), 3277–3294.

18 M. Daoudy, N. Gouitaa, F. Z. Ahjyaje, T. Lamcharfi and F. Abdi, Synthesis, structural study, optical, dielectric, and electrical properties of a new lead-free C2H5NH3BaCl3 organic–inorganic hybrid perovskite, *J. Mater. Res.*, 2024, **39**(9), 1411–1424.

19 J. Salgado-Beceiro, S. Castro-García, M. Sánchez-Andújar and F. Rivadulla, Motional Narrowing of Electron Spin Resonance Absorption in the Plastic-Crystal Phase of [(CH3)4N]FeCl4, *J. Phys. Chem. C*, 2018, **122**(48), 27769–27774.

20 C. Sanchez, C. Boissiere, S. Cassaignon, C. Chaneac, O. Durupthy, M. Faustini, *et al.*, Molecular Engineering of Functional Inorganic and Hybrid Materials, *Chem. Mater.*, 2014, **26**(1), 221–238.

21 V. Thirumal, N. Mahato, K. Yoo and J. Kim, High performance Li-ion battery-type hybrid supercapacitor devices using antimony based composite anode and Ketjen black carbon cathode, *J. Energy Storage*, 2023, **61**, 106756.

22 V. Adimule, B. C. Yallur, M. Challa and R. S. Joshi, Synthesis of hierarchical structured Gd doped α-Sb2O4 as an advanced nanomaterial for high performance energy storage devices, *Heliyon*, 2021, 7(12), 8541, **https://www.cell.com/heliyon/abstract/S2405-8440(21)02644-X**.

23 D. Wu, W. Sang, B. Huo, J. Wang, X. Wang, C. Chen, *et al.*, Highly crystalline lead-free Cs3Sb2Br9 perovskite

microcrystals enable efficient and selective photocatalytic oxidation of benzyl alcohol, *J. Catal.*, 2022, **408**, 36–42.

24 P. Saha, S. Singh and S. Bhattacharya, Higher Efficiency and Stability in Planar Homojunction Hybrid Antimony (MA3Sb2I9)- Based Perovskite Solar Cells, *IEEE J. Quantum Electron.*, 2023, **59**(5), 1–8.

25 A. Le Bail, H. Duroy and J. L. Fourquet, Ab-initio structure determination of LiSbWO6 by X-ray powder diffraction, *Mater. Res. Bull.*, 1988, **23**(3), 447–452.

26 J. Rodríguez-Carvajal, Recent advances in magnetic structure determination by neutron powder diffraction, *Phys. B*, 1993, **192**(1), 55–69.

27 M. A. Spackman and J. J. McKinnon, Fingerprinting intermolecular interactions in molecular crystals, *CrystEngComm*, 2002, **4**(66), 378–392.

28 P. R. Spackman, M. J. Turner, J. J. McKinnon, S. K. Wolff, D. J. Grimwood, D. Jayatilaka, *et al.*, CrystalExplorer: a program for Hirshfeld surface analysis, visualization and quantitative analysis of molecular crystals, *J. Appl. Crystallogr.*, 2021, **54**(3), 1006–1011.

29 K. Iben Nassar, F. Tayari, M. Slimi, N. Rammeh, A. Njeh, T. S. Soreto, *et al.*, Temperature- and frequency-dependent dielectric and impedance spectroscopy of double perovskite oxide BiBa0.5Ag0.5Ni2O6 electronic material, *J. Mater. Sci.: Mater. Electron.*, 2023, **34**(3), 216.

30 M. Wojtaś, R. Jakubas, Z. Ciunik and W. Medycki, Structure and phase transitions in [(CH3)4P]3[Sb2Br9] and [(CH3)4P]3[Bi2Br9], *J. Solid State Chem.*, 2004, **177**(4), 1575–1584.

31 C. F. Macrae, I. J. Bruno, J. A. Chisholm, P. R. Edgington, P. McCabe, E. Pidcock, *et al.*, Mercury CSD 2.0 – new features for the visualization and investigation of crystal structures, *J. Appl. Crystallogr.*, 2008, **41**(2), 466–470.

32 M. Wojtas, R. Jakubas, Z. Ciunik and W. Medycki, Structure and phase transitions in [(CH{sub 3}){sub 4}P]{sub 3}[Sb{sub 2}Br{sub 9}] and [(CH{sub 3}){sub 4}P]{sub 3}[Bi{sub 2}Br{sub 9}], *J. Solid State Chem.*, 2004, **177**, 1575, **https://www.osti.gov/etdeweb/biblio/20487675**.

33 M. Khalfa, A. Oueslati, K. Khirouni, M. Gargouri, A. Rousseau, J. F. Bardeau, *et al.*, Structural phase transitions in [(CH3)4P]3M2Cl9 (M = Bi and Sb) hybrid compounds revealed by temperature-controlled Raman spectroscopy and X-ray diffraction, *J. Phys. Chem. Solids*, 2023, **176**, 111227.

34 V. Varma, R. Bhattacharjee, H. N. Vasan and C. N. R. Rao, Infrared and Raman spectroscopic investigations of methylammonium haloantimonates(III), [N(CH3)4−nH*n*]3Sb2X9 (*n* = 0–3, X = Cl or Br), through their phase transitions, *Spectrochim. Acta, Part A*, 1992, **48**(11), 1631–1646.

35 K. Nakamoto *Infrared and Raman Spectra of Inorganic and Coordination Compounds, Part B: Applications in Coordination, Organometallic, and Bioinorganic Chemistry*. John Wiley & Sons; 2009. p. 423.

36 M. Wojtaś, R. Jakubas and J. Baran, Vibrational study of the ferroelastic phase transition in [(CH3)4P]3[Bi2Cl9], *Vib. Spectrosc.*, 2005, **39**(1), 23–30.

37 U. K. N. Din, M. A. Mohamed, M. M. Salleh and T. H. T. Aziz, Effect of temperature on the formation of highly crystalline lead-free perovskite Cs3Sb2Br9 hexagonal microdisks, *J. Mater. Sci.: Mater. Electron.*, 2022, **33**(17), 13625–13633.

38 A. Ghoudi, I. Chaabane, R. Naouari, A. Aydi, A. Oueslati, E. Dhahri, *et al.*, Optical and electric properties of the organic-inorganic hybrid bis(2-amino-5-picolinium) Tetrachlorocobaltate(II) [(C6H9N2)2CoCl4], *Inorg. Chem. Commun.*, 2024, **168**, 112925.

39 Y. Moualhi, H. Rahmouni and F. Bahri, Doublet doped titanate ferroelectric system for capacitors and NTC thermistor applications, *Sens. Actuators, A*, 2024, **377**, 115596.

40 I. Dhouib, A. Ouasri, P. Guionneau and Z. Elaoud, A new organic-inorganic hybrid compound based on sulfate: Structural characterization, DFT study, Hirshfeld analysis, and electrical, vibrational and thermal properties, *J. Phys. Chem. Solids*, 2022, **165**, 110654.

41 A. Feteira, Negative Temperature Coefficient Resistance (NTCR) Ceramic Thermistors: An Industrial Perspective, *J. Am. Ceram. Soc.*, 2009, **92**(5), 967–983.

42 M. B. Bechir, M. Akermi and H. J. Alathlawi, Understanding charge transport and dielectric relaxation properties in lead-free Cs 2 ZrCl 6 nanoparticles, *RSC Adv.*, 2024, **14**(20), 14221–14232.

43 S. Karmakar and D. Behera, Non-overlapping small polaron tunneling conduction coupled dielectric relaxation in weak ferromagnetic NiAl2O4, *J. Phys.:Condens. Matter*, 2019, **31**(24), 245701.

44 I. Garoui, S. Hajlaoui, I. Kammoun, A. Ouasri, J. Lhoste, H. Abid, *et al.*, Synthesis, crystal structure, BFDH morphology, Hirshfeld surface analysis and electrical characterization of the new bi-(2-amino-5-methylpyridinium) hexa-chlorostannate compound, *Phys. E*, 2024, **158**, 115897.

45 A. Ghoudi, K. B. Brahim, H. Ghalla, J. Lhoste, S. Auguste, K. Khirouni, *et al.*, Crystal structure and optical characterization of a new hybrid compound, C 6 H 9 N 2 FeCl 4 , with large dielectric constants for field-effect transistors, *RSC Adv.*, 2023, **13**(19), 12844–12862.

46 W. Hizi, M. Gassoumi, H. Rahmouni, A. Guesmi, N. Ben Hamadi and E. Dhahri, Effect of Sintering Temperature and Polarization on the Dielectric and Electrical Properties of La0.9Sr0.1MnO3 Manganite in Alternating Current, *Materials*, 2022, **15**(10), 3683.

47 A. Ghosh and D. Chakravorty, AC conduction in semiconducting CuO-Bi2O3-P2O5 glasses, *J. Phys.: Condens. Matter*, 1990, **2**(24), 5365.

48 X. L. Cleac'h, Lois de variations et ordre de grandeur de la conductivité alternative des chalcogénures massifs non cristallins, *J. Phys.*, 1979, **40**(4), 417–428.

49 G. E. Pike, ac Conductivity of Scandium Oxide and a New Hopping Model for Conductivity, *Phys. Rev. B*, 1972, **6**(4), 1572–1580.

50 P. Yadav and A. Sharma, Temperature and frequency dependence of AC conductivity of new quaternary Se-Te-Bi-

Pb chalcogenide glasses, *AIP Conf. Proc.*, 2016, **1728**(1), 020189.

51 K. L. Ngai and C. León, Recent advances in relating macroscopic electrical relaxation data to microscopic movements of the ions in ionically conducting materials, *Solid State Ionics*, 1999, **125**(1), 81–90.

52 A. Molak, M. Paluch, S. Pawlus, J. Klimontko, Z. Ujma and I. Gruszka, Electric modulus approach to the analysis of electric relaxation in highly conducting (Na0.75Bi0.25)(Mn0.25Nb0.75)O3 ceramics, *J. Phys. D: Appl. Phys.*, 2005, **38**(9), 1450.

53 S. B. Yahya and B. Louati, Characterization of the structure and conduction behavior of overlapping polaron tunnel of dipotassium zinc orthogermanate, *J. Alloys Compd.*, 2021, **876**, 159972.

54 I. Gharbi, A. Ghoudi, I. Kammoun, A. Mahmoud and A. Oueslati, Dielectric relaxation and charge transfer mechanism of the inorganic perovskite CsHgCl3, *Inorg. Chem. Commun.*, 2024, **166**, 112565.

55 A. García-Fernández, J. M. Bermúdez-García, S. Castro-García, A. L. Llamas-Saiz, R. Artiaga, J. López-Beceiro, *et al.*, Phase Transition, Dielectric Properties, and Ionic Transport in the [(CH3)2NH2]PbI3 Organic–Inorganic Hybrid with 2H-Hexagonal Perovskite Structure, *Inorg. Chem.*, 2017, **56**(9), 4918–4927.

56 P. P. Shi, Q. Ye, Q. Li, H. T. Wang, D. W. Fu, Y. Zhang, *et al.*, Novel Phase-Transition Materials Coupled with Switchable Dielectric, Magnetic, and Optical Properties: [(CH3)4P][FeCl4] and [(CH3)4P][FeBr4], *Chem. Mater.*, 2014, **26**(20), 6042–6049.

57 M. F. Mostafa, ShS. El-khiyami and S. K. Alal, Structure, thermal, and impedance study of a new organic–inorganic hybrid [(CH2)7(NH3)2]CoCl4, *J. Phys. Chem. Solids*, 2018, **118**, 6–13.

58 N. Mahfoudh, K. Karoui, M. Gargouri and A. BenRhaiem, Optical and electrical properties and conduction mechanism of [(CH3)2NH2]2CoCl4, *Appl. Organomet. Chem.*, 2020, **34**(3), e5404.